Article

DCGAN-Based Feature Augmentation: A Novel Approach for Efficient Mineralization Prediction Through Data Generation

Soran Qaderi [1], Abbas Maghsoudi [1,*], Amin Beiranvand Pour [2,*], Abdorrahman Rajabi [3] and Mahyar Yousefi [4]

[1] Department of Mining Engineering, Amir Kabir University of Technology, Tehran 1591634311, Iran; soranqaderi@aut.ac.ir

[2] Institute of Oceanography and Environment (INOS), Higher Institution Center of Excellence (HICoE) in Marine Science, University Malaysia Terengganu (UMT), Kuala Nerus 21030, Terengganu, Malaysia

[3] School of Geology, College of Science, University of Tehran, Tehran 1417935840, Iran; rahman.rajabi@ut.ac.ir

[4] Faculty of Engineering, Malayer University, Malayer 6571995863, Iran; m.yousefi.eng@gmail.com

[*] Correspondence: a.maghsoudi@aut.ac.ir (A.M.); beiranvand.pour@umt.edu.my (A.B.P.)

Abstract: This study aims to improve the efficiency of mineral exploration by introducing a novel application of Deep Convolutional Generative Adversarial Networks (DCGANs) to augment geological evidence layers. By training a DCGAN model with existing geological, geochemical, and remote sensing data, we have synthesized new, plausible layers of evidence that reveal unrecognized patterns and correlations. This approach deepens the understanding of the controlling factors in the formation of mineral deposits. The implications of this research are significant and could improve the efficiency and success rate of mineral exploration projects by providing more reliable and comprehensive data for decision-making. The predictive map created using the proposed feature augmentation technique covered all known deposits in only 18% of the study area.

Keywords: deep convolutional generative adversarial network; evidence layer; feature augmentation; decision-making

1. Introduction

In recent years, mineral prospectivity mapping (MPM) has employed various exploration methods to find promising areas for certain types of mineralization [1–7]. Among these, machine learning (ML) and deep learning (DL) algorithms have become very important [8–14]. Researchers have continuously explored and proposed innovative approaches to find mineralization and reduce uncertainties [15–19]. Efforts have also focused on the optimization of hyperparameters to develop efficient predictive models and combine multiple algorithms to improve prediction accuracy [20–24].

Despite the progress, one of the major challenges in DL algorithms remains the scarcity of feature datasets. The efficiency of a neural network is directly proportional to the amount and variety of its input data. A well-trained network enriched with extensive data is better able to make realistic and reliable predictions, ensuring greater confidence in its predictive capabilities [25–27]. Therefore, it is essential to develop strategies to expand the pool of input datasets through reliable methods. Feature augmentation techniques can generate new and useful features from existing data, improving the model's ability to detect hidden patterns without introducing bias.

This study proposes to gain new insights from existing mineral exploration data by creating evidence layers from different geoscience domains, including lithological, geochemical, structural, and remote sensing data. These layers capture the underlying

geologic patterns and characteristics, even though they require a significant amount of preparation. Our novel approach augments the features by generating synthetic features. These synthetic features, referred to as "evidence layers", capture additional information beyond the primary features. By using these layers, we aim to improve the model's ability to learn from different examples. These layers provide additional clues such as geological features, geochemical anomalies, and structural patterns and improve the model's ability to distinguish between prospective and non-prospective areas.

In this study, aiming at generating more informative evidence layers and extracting additional information from complex geologic patterns, we have chosen the Deep Convolutional Generative Adversarial Network (DCGAN) architecture. This architecture utilizes Convolutional Neural Network (CNN), which are effective for image processing and capable of extracting complex and important features from images. These convolutional layers in DCGAN help produce high-quality images and enable the generation of realistic images from random noise. DCGANs have been successfully applied in various domains [28–33]. This paper focuses on the implementation of feature augmentation using DCGAN and the subsequent prediction of high-potential Mississippi Valley-type (MVT) Pb-Zn mineralization areas in western Semnan, Iran. A Random Forest (RF) model is employed to illustrate the proposed method and demonstrate its performance in MPM.

2. Geological Framework of the Study Area and Conceptual Modeling

The study area is located in western Semnan, Iran, and includes a 1:100,000 scale geologic map of the Semnan region. This area includes parts of both the Alborz and Central Iran zones, which are separated by the Semnan Fault within the district. The northern part of the study area belongs to the Alborz zone, which consists of shale, green sandstone and tuff (Kahar Formation), volcanic rocks, shale, and carbonaceous sandstones (Shemshak Formation). The southern part, on the other hand, belongs to the Central Iran Zone and consists of continental or shallow marine sediments, shale and sandstone limestones, sandstone and swamp sediments, marls, and conglomerates (Neogene units) [34–36]. The Semnan Quadrangle hosts a variety of minerals, some of which are mined locally on a modest scale. Fluorine deposits occur in several places in the Alborz Mountains, especially in the uppermost limestone layers of the Elika Formation. In the Upper Cretaceous limestone, galena veins can be found in the mountains of Oran and Sefid Kouh, and barite veins can be found in the southern limestones of Shahmirzad. In addition, several occurrences of Pb-Zn mineralization, especially those classified as MVT, have been documented [37]. Figure 1b shows the geographical distribution of 16 recognized MVT Pb-Zn deposits within the study area.

MVT Pb–Zn deposits are a diverse group of epigenetic deposits that form from concentrated basinal fluids at temperatures between 75 °C and 200 °C and are typically found in carbonate platforms without a direct volcanic context [37–40]. These deposits are mainly found in passive tectonic margins within carbonate sequences. They are found along basin margins, in overthrust belts of foreland basins, and occasionally within carbonate platforms in extensional zones. These deposits are thought to have formed from ore-forming fluids that migrated through foreland basins and precipitated metal sulfides from nearby orogenic belts due to gravitational forces. These deposits are typically hosted in dolomite and limestone formations and exhibit textures such as displacement, cavity filling, and unconformity. The most important minerals include sphalerite, galena, pyrite, marcasite, dolomite, and calcite. Dolomitization is a major alteration in the MVT Pb-Zn mineralization [37,40–45].
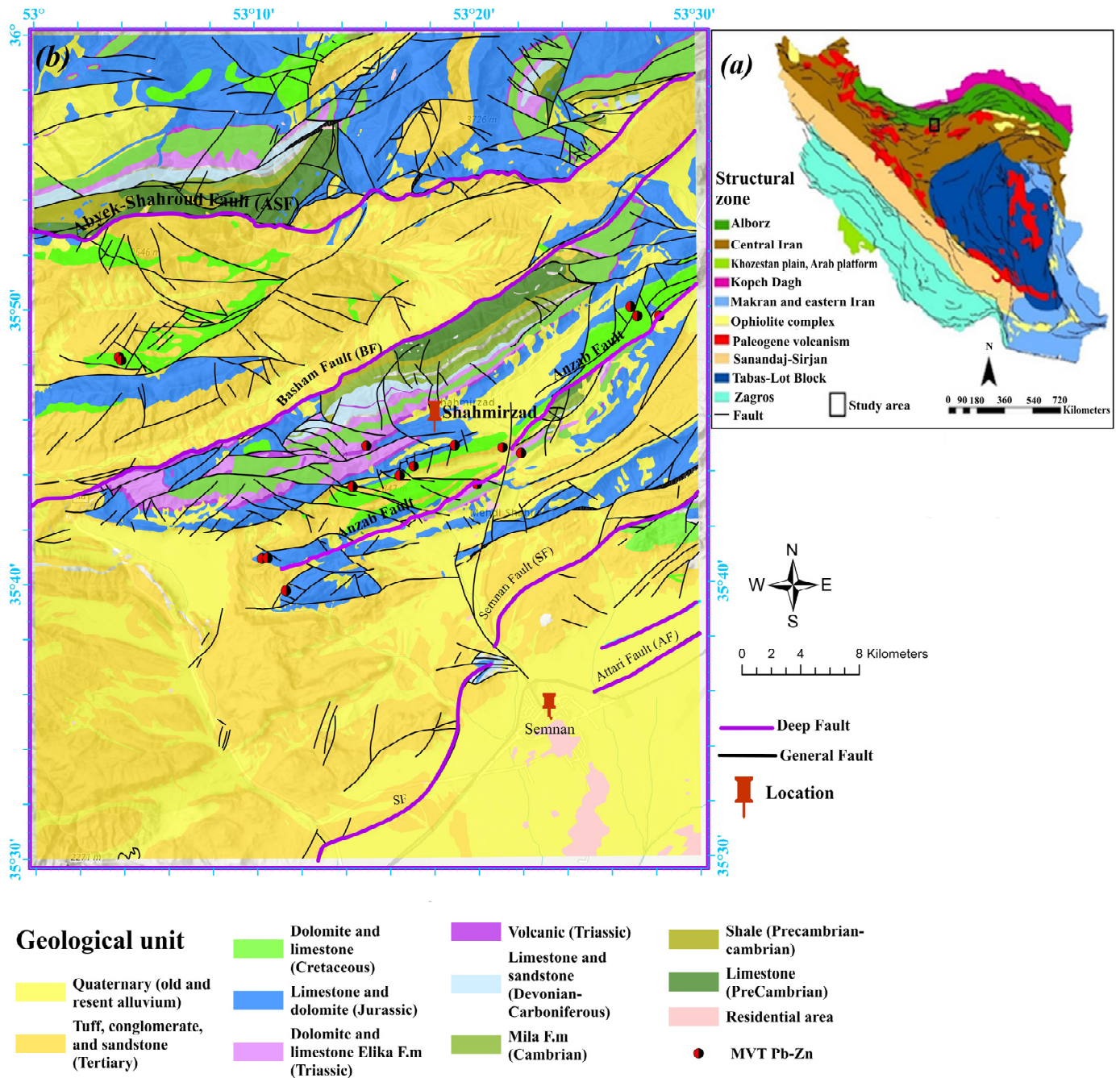
Figure 1. (**a**) Location of the study area in Iran, (**b**) simplified geological map of the study area.

3. Feature Analysis

In the context of MPM, several geospatial variables control the corresponding ore mineralization. These variables may be tectonic forces, fluid composition, fracture systems, and/or compositional locations. Concerning MVT Pb-Zn mineralization, we have used geochemical, structural, lithological, and remote sensing information to create appropriate and informative features that capture the underlying patterns and geological characteristics.

The importance of the investigation of geochemical data for the successful identification of promising areas and, thus, for the modeling of mineralization has been confirmed in several studies [46–48]. Therefore, the geochemical maps of Pb, Zn, and Ba are considered as geochemical signatures of indicator elements after the necessary preprocessing of the geochemical data, including the substitution of sensor values and overcoming the closure effect of the data.

Faults and fractures play a crucial role in the formation of MVT deposits as they provide the pathway for basinal brines to move through the Earth's crust and interact with the host rocks. Movement along these structures can create cavities and open spaces where mineralization takes place. Ore-bearing fluids are channeled through fault corridors and then trapped and circulated further through permeable corridors in suitable host rocks. These processes enhanced the conduction of ore-forming fluids and subsequent supergene and oxidative processes [49–52]. Considering the importance of faults for the transfer of extracted metals through basinal brines to suitable host rocks and subsequent MVTPb-Zn deposition, we used distance distribution analysis [49,53–55] to identify the major faults responsible for the movement of fluids. For this purpose, the different faults in the study area were categorized into four main directions: N-S, E-W, NW-SE, and NE-SW (Figure 2a). We also created a rose diagram showing the faults in western Semnan (Figure 2b). Distance maps were created for all four orientations (Figure 3). Spatial correlations between the MVTPb-Zn deposits and these structural features were then evaluated using the distance distribution analysis method. Accordingly, NE-SW striking faults showed significant positive spatial associations with the sought mineralization type in western Semnan. In addition, NW-SE and also E-W striking faults showed a high correlation with the mineralization encountered. Therefore, the intersections of faults and the NE-SW striking faults were identified as the main structural controlling factors in the deposition of MVT Pb-Zn in the study area. To demonstrate their role in mineralization, we created a fault density map aligned with the distance map of NE-SW trending faults as structural information layers.
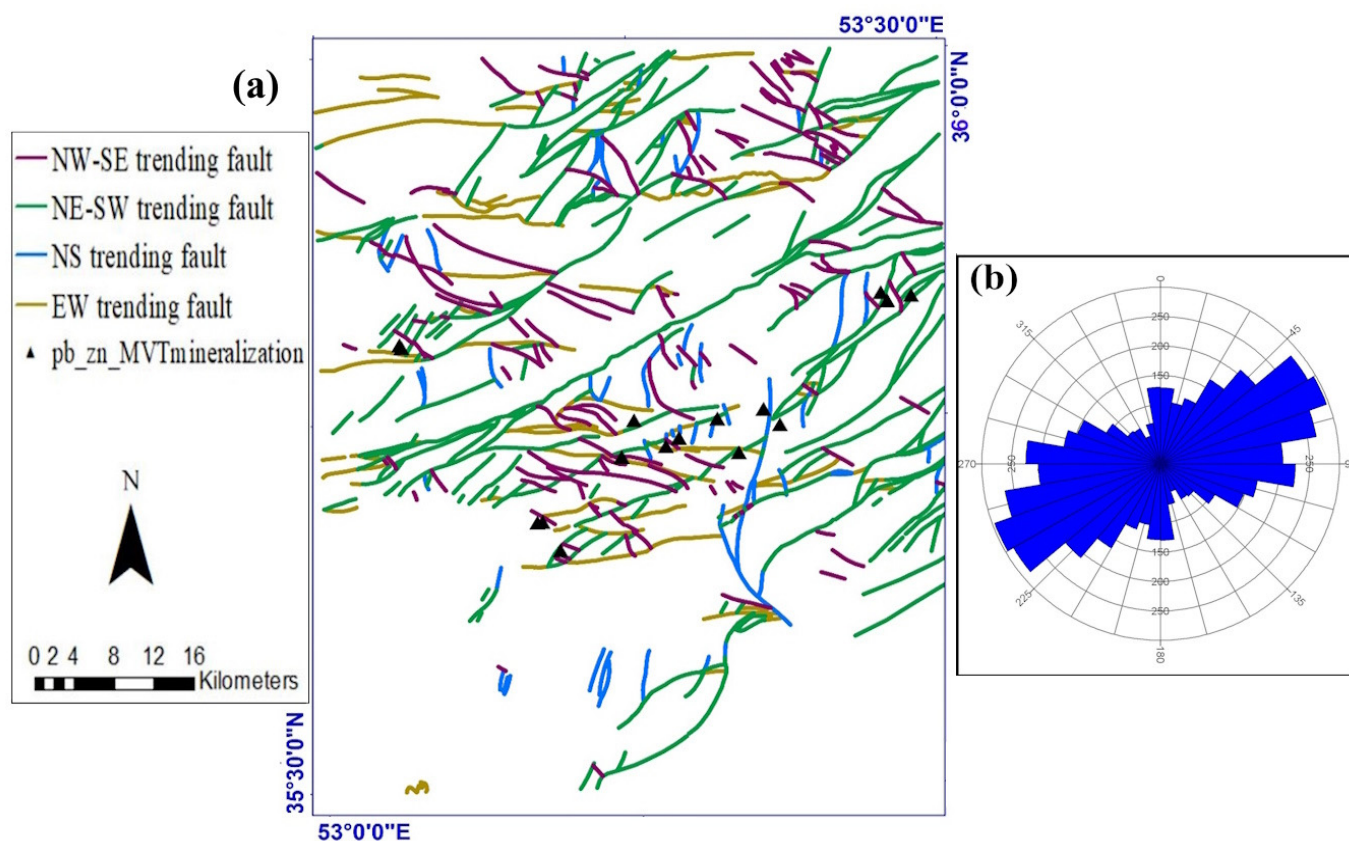
Figure 2. (**a**) Four main orientations of faults in the study area, (**b**) rose diagram demonstrating fault trending in the district.
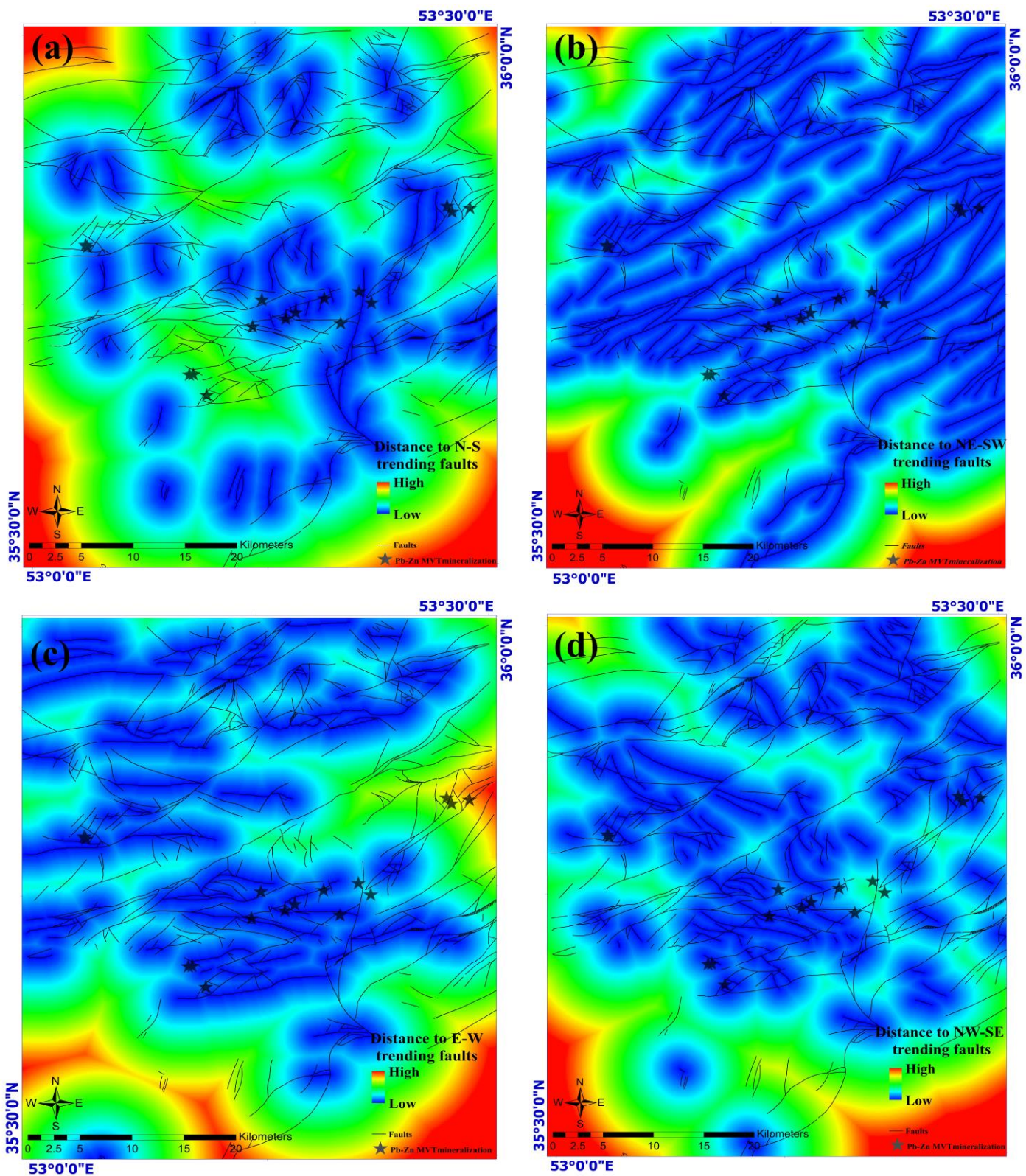
Figure 3. Distance maps of (**a**) N-S, (**b**) NE-SW, (**c**) E-W, and (**d**) NW-SE trending faults in the study area.

The presence of a suitable host rock is a fundamental prerequisite for the enriched fluid to concentrate and for mineralization to take place. In the western Semnan region, MVTPb-Zn mineralization occurs in Permian–Cretaceous dolomite and limestone [37,40,41]. In addition, various studies emphasize that dolomite and limestone provide favorable conditions for focusing fluids due to their high porosity and permeability. They are suitable

chemical and physical traps [37,41,49,56–60]. Therefore, we separated the lithological units of the Permian–Cretaceous dolomite and limestone from the digitized geological map of Semnan at a scale of 1:100,000. Then, a map with continuous distances was created and considered as one of the information layers.

The application of remote-sensing-based processing techniques to detect hydrothermal alteration in mineral exploration is undeniable [61–70]. Enriched fluids containing ions such as Mg^{2+}, when trapped in suitable host rocks, lead to an exchange of dolomite with the original calcite in the rock, changing its composition and causing dolomitization alteration to occur. Dolomitization often occurs on a large scale and results in distinct dolomite mineral grains that are larger than the original calcite crystals in the limestone. Due to the importance of detecting dolomite alterations in identifying MVT Pb-Zn mineralization, a map of dolomite zones was created by applying image processing techniques such as a band ratio, principal component analysis, spectral angle mapper, and band math methods to the ASTER dataset. Subsequently, the results were combined using the fuzzy gamma algorithm. All features were rasterized with a size of 150×150 cells. In addition, the gridded features were transformed into the range [0, 1] using a logistic function [71–78].

4. Methods

4.1. General Workflow

In this study, we have prepared seven layers of information derived from various geological sciences, including lithology, remote sensing, structural analysis, and geochemistry. These original evidence layers (OELs) collectively represent the intricate geological features of the district. Our goal is to augment the number of these features and thereby improve our understanding of the underlying patterns and geological information. By revealing more of the complexity of the geological patterns, we get closer to identifying truly prospective areas. Therefore, we aim to generate a synthetic layer for each layer of evidence. Consequently, we will have seven Generated Evidence Layers (GELs), which will increase the diversity and richness of our dataset. Figure 4 shows a schematic workflow of the method used in this study.
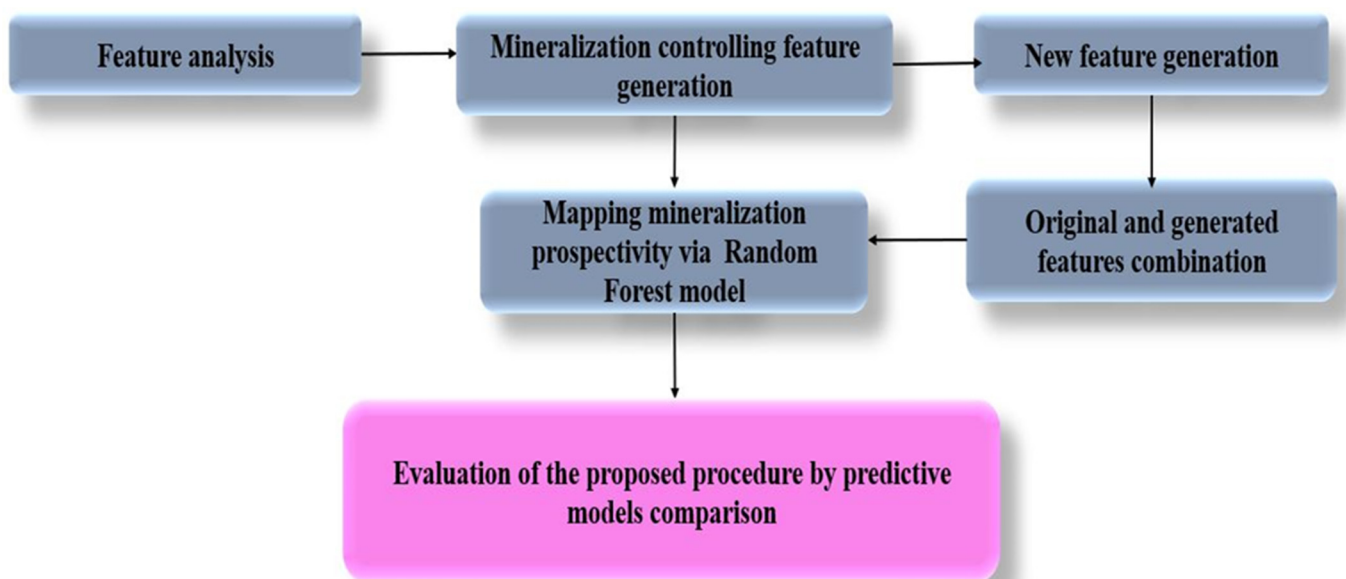

Figure 4. A schematic workflow of the procedure used in this study.

4.2. Deep Convolutional Generative Adversarial Network (DCGAN)

DCGAN is a generative model that combines Deep Convolutional Neural Networks (CNNs) with adversarial training. Generative Adversarial Networks (GANs) [28,79,80] consist of two neural networks: Generator and Discriminator. The first generates new data (e.g., images), and the second discriminates the generated data from real data. The generator and the discriminator are trained simultaneously in an adversarial manner. The generator gets better at creating realistic data, while the discriminator gets better at distinguishing real from fake data. Training continues until the discriminator can no longer distinguish between real and generated data. GANs gradually improve their performance through this dynamic interaction and generate synthetic data that closely resemble real-world examples [80,81]. DCGANs specifically use CNNs in both the generator and the discriminator. They are commonly used for image generation, style transfer, and unsupervised representation learning. The incorporation of deep CNNs into GANs makes DCGANs more robust and effective for image generation as they can extract complex, important features from images [33].

4.3. Random Forest (RF)

The RF algorithm is a robust and versatile ML technique used for both classification and regression tasks [82,83]. It works by creating a large number of decision trees during the training phase and outputting the class that corresponds to the mode of the classes (classification) or the mean prediction (regression) of each tree. The algorithm begins by creating multiple subsets of the original dataset through a process called bootstrapping. Each subset is created by randomly selecting data points with substitutions, ensuring that some data points can appear multiple times in a subset while others cannot appear at all. A decision tree is created for each subset. During the construction of each tree, a random subset of features is selected at each node to determine the best split. This randomness helps to create diverse trees that are less likely to overfill the training data. Once all trees are created, the algorithm summarizes their predictions. For classification tasks, each tree votes for a class, and the class with the most votes is selected as the final prediction. For regression tasks, the predictions of all trees are averaged to obtain the final output. By averaging multiple trees, the RF algorithm reduces the risk of overfitting that often occurs with single decision trees. RF can effectively handle missing values by using the median of the observed values in the training data. The algorithm provides estimates of feature importance that can be useful for understanding the underlying data and for feature selection. RF is used in various domains such as finance, healthcare, marketing, and MPM due to its high accuracy and ability to handle large datasets with higher dimensionality [40,84–86]. It is particularly effective in scenarios where the relationship between the features and the target variable is complex and non-linear. The RF algorithm is a powerful tool for predictive modeling that offers a balance between bias and variance and provides reliable predictions. Its ability to handle both classification and regression tasks, as well as its robustness to overfitting, make it a popular choice among data scientists and researchers.

5. Analysis and Results

5.1. Feature Augmentation by DCGAN

To generate new features by DCGAN, we need to preprocess our existing features. For this purpose, we have reshaped them to the same dimension. All features had the size (1480 × 1800). This size is very large for image processing and requires a lot of time and powerful processing equipment; therefore, we need to reshape all layers into smaller dimensions to avoid complex and time-consuming processing. Therefore, we converted all existing features into dimensions (64 × 64) and then normalized the pixel values

to a common range (0, 1) to facilitate training. After proper preparation, we designed the architecture for both the generator and discriminator networks. When designing the DCGAN generator, we used convolutional layers to convert the noise into realistic-looking data and leaky ReLU activation functions, which are commonly used to prevent the gradients from disappearing during training. For the design of the discriminator DCGAN, we also used convolutional layers to process the input data and, again, the leaky ReLU activation function. In the training process, the generator aims to fool the discriminator by generating realistic data; on the other hand, the discriminator learns to distinguish real from synthetic data. We used a binary cross-entropy loss function to drive the training process. Experimenting with hyperparameters such as the learning rate, batch size, and network architecture, as well as monitoring the training progress using metrics such as the loss and visual inspection of the generated samples, resulting in an ideal model training. Effective model training yields generated samples that serve as synthetic evidence layers for feature augmentation.

5.2. Augmented Dataset

After successfully implementing the DCGAN model, we created seven new features. For the evaluation of the GELs, we visually compared them with the OELs and validated their usefulness in our mineral exploration research. These generated features show a satisfactory fit to their originals. Additionally, to assess the quality of the data generated by the DCGAN model, Probability Density Function (PDF) plots for both the original and generated data were created and compared [87]. The results demonstrate a significant overlap between the original and generated data, indicating that the DCGAN model has successfully captured and replicated the distribution of the original data (Figure 5a). Figure 5b,c shows the original features and the features generated with the DCGAN algorithm.

5.3. Data Augmentation Practical Implication

Mineral Prospectivity Mapping (MPM)

To create an MVTPb-Zn mineralization prediction map via the proposed strategy, we combined OELs and GELs to enhance the identified geological features. The combined features were used for model training and mineralization prediction. The model was trained using a dataset with 14 features and two labels: label 1 for the presence of mineralization and label 0 for samples without mineralization. To prepare the labels of this dataset, we placed a 1500 m buffer around the location of each of the 16 known deposits and labeled them with one. We also randomly selected 16 points far from the known deposits, placed a 1500 m buffer around them, and labeled them 0. Following extracting geospatial features of mineralization and non-mineralization points, this labeling workflow resulted in 3045 positive samples (labeled 1) and 3181 negative samples (labeled 0). We then collected 3045 samples from each category to avoid imbalance issues between positive and negative samples. A total of 80% of this dataset was used for training and 20% for testing.

To further demonstrate the superiority of the proposed strategy, we also used the RF model to predict mineralization using only the real features. For this purpose, the model was trained with seven features and two labels, following a similar labeling procedure previously described.

(a)
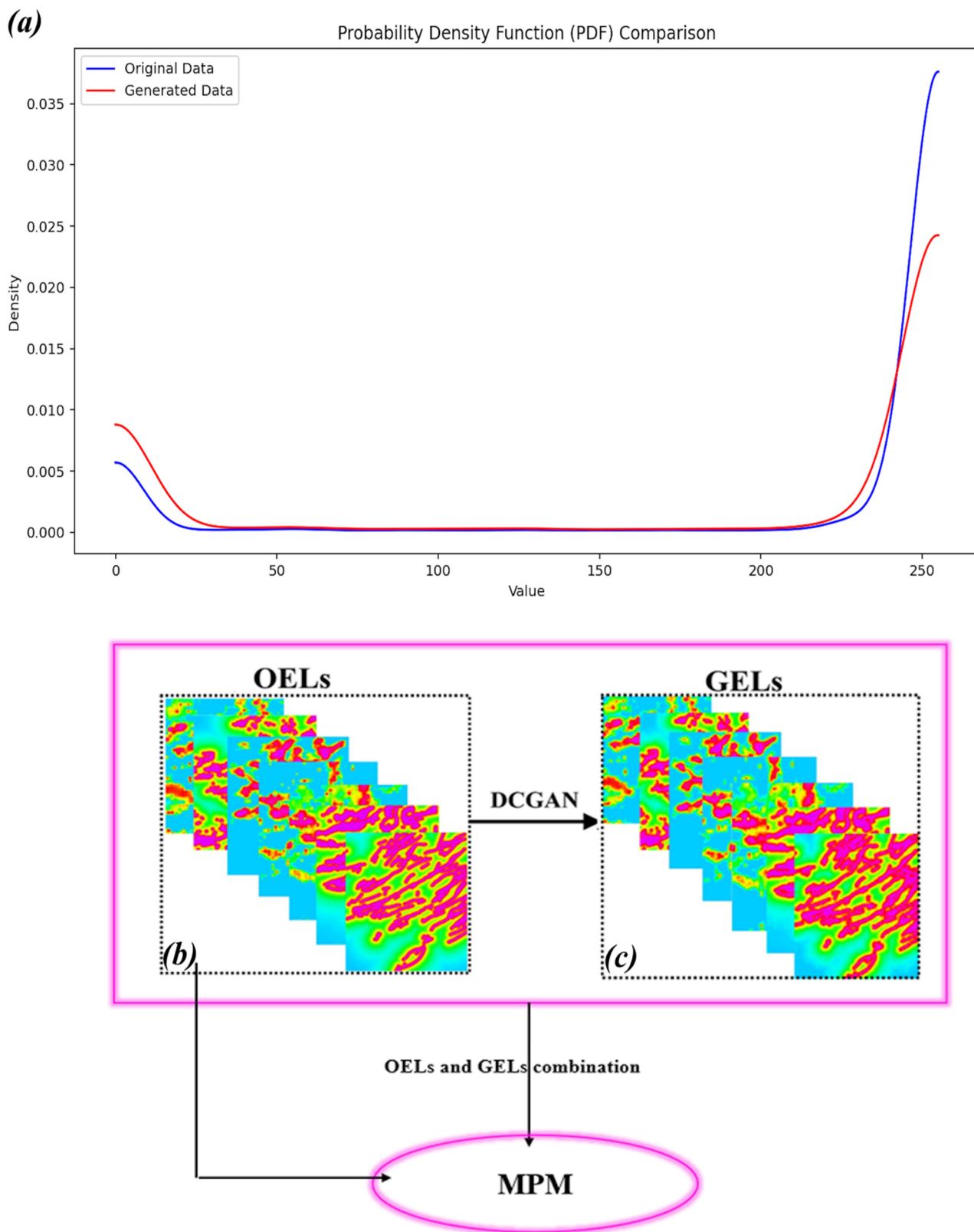
Figure 5. (**a**) Comparison of the PDF for Original and Generated Data, (**b**) Original mineralization controlling features, (**c**) Generated features through DCGAN.

To evaluate the prediction capability of the models, we utilized the test data and assessed the R-squared (R^2) score [88] and the area under the precision–recall curve (AUPRC) [89]. The results demonstrated that the proposed model, which leveraged DCGAN-based feature augmentation, achieved an R^2 score of 0.92 and an AUPRC of

0.99. In contrast, the model trained solely on the existing features obtained an R^2 score of 0.87 and an AUPRC of 0.98. These results underscore the robustness of the RF model enhanced by the feature augmentation technique. The appropriate RF tuning hyperparameters of the models are listed in Table 1. By training appropriately and using the developed model, we created a prediction map for MVT Pb-Zn mineralization in western Semnan, as shown in Figure 6a. Figure 6b shows the prediction map created based on the real features only. In addition, a graphical explanation of the methodology applied in this study has been demonstrated in Figure 7.

Table 1. Characteristics of the model used in this study.

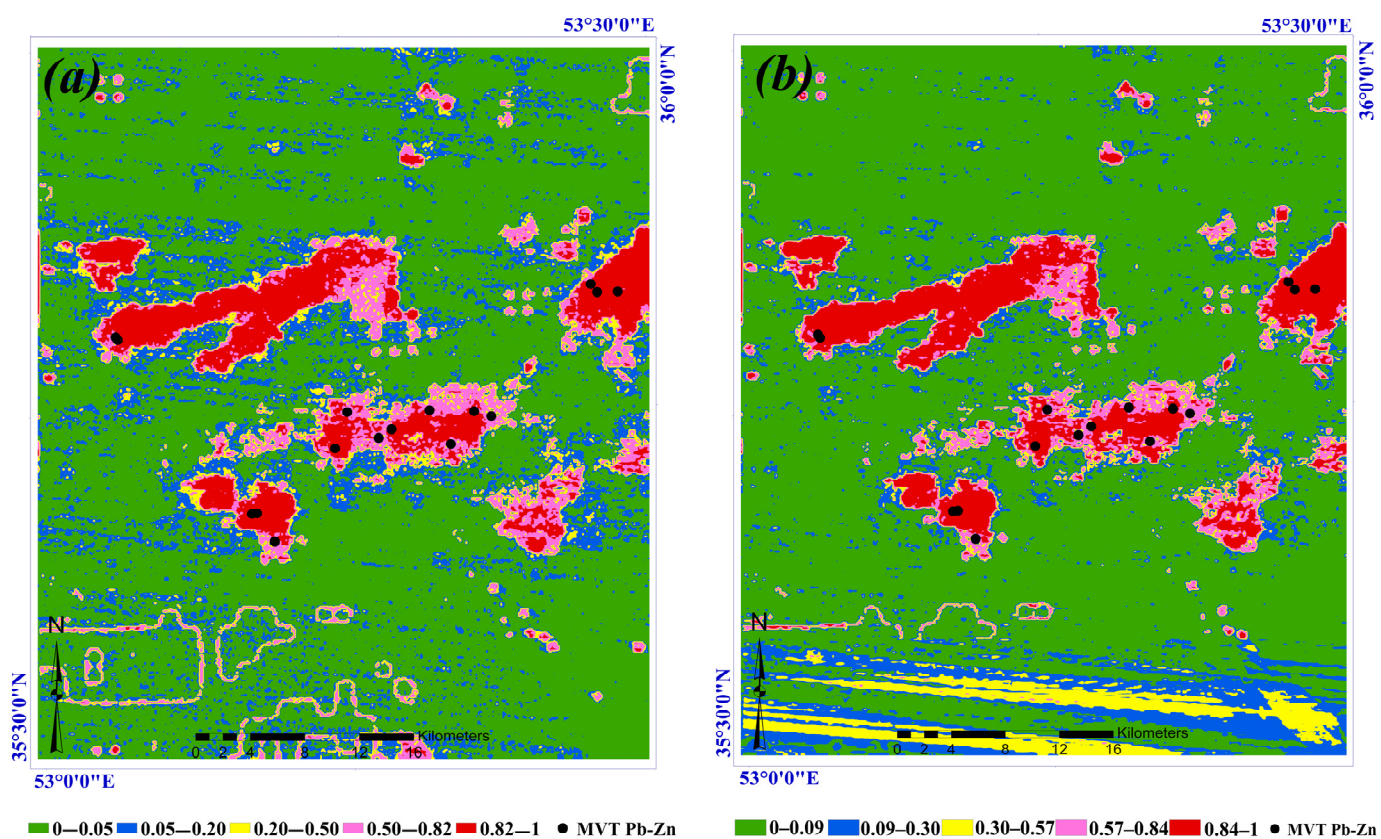| Characteristic	Value	Explanation
Model	Random Forest	A machine learning model is used for regression/classification tasks, which builds multiple decision trees and merges them to get a more accurate and stable prediction.
Number of Estimators	300	The number of trees in the forest. More trees can improve performance but also increase computation time.
Random State	42	A seed used by the random number generator to ensure reproducibility of the results.

Figure 6. Prediction map obtained by RF based on (**a**) DCGAN-based augmented features, and (**b**) real features.

Data preprocessing

| Input Features: Original dimensions (1480×1800) | Resizing: Convert to smaller dimensions (64×64) using tf. image. resize | Normalization: Pixel values normalized to the range (0, 1) |

DCGAN architecture

Generator

Dense input reshaped to 8×8×256 feature map

Transposed convolutional layers with strides and padding

Batch normalization

Leaky ReLU activation functions

Discriminator

Convolutional layers with strides and padding

Leaky ReLU activation functions

Dropout layers to mitigate overfitting

Flatten and dense layers for final output

Training process

Generator: Tries to create convincing synthetic features

Discriminator: Improves its ability to differentiate between real and synthetic

Loss Functions:

Generator loss: cross entropy with fake output

Discriminator loss: cross entropy with real and fake output

Optimization:

Adam optimizers for both generator and discriminator

Training with Gradient Tape to calculate and apply gradients

Hyperparameters:

Learning rate: 1×10^{-4}

Batch size: 256

Epochs: 50

Monitoring: Training progress using metrics like loss and visual inspection of samples

Feature Generation:

| Generate Synthetic Features (GELs) using noise input and trained generator | Resize GELs back to Original Size (1480×1800) for consistency with real features (OELs) |

Save GELs using the save raster function to ensure proper geospatial alignment

Evaluation: Visually compare GELs with OELs and validate their usefulness in MPM

Combine OELs and GELs to create a comprehensive feature dataset

Labeling

| Mineralization: 16 points of known deposits | Non-mineralization: 16 points randomly far from known deposits |
| 1500-meter buffer around known mineralization for labeling | 1500-meter buffer around non-mineralization for labeling |

Dataset preparation for RF training:

| DCGAN-based augmented dataset (augmented features and two labels) | Original dataset (original features and two labels) |

Data Split by sklearn: 80% for training, 20% for testing

Model training

Evaluation by test data

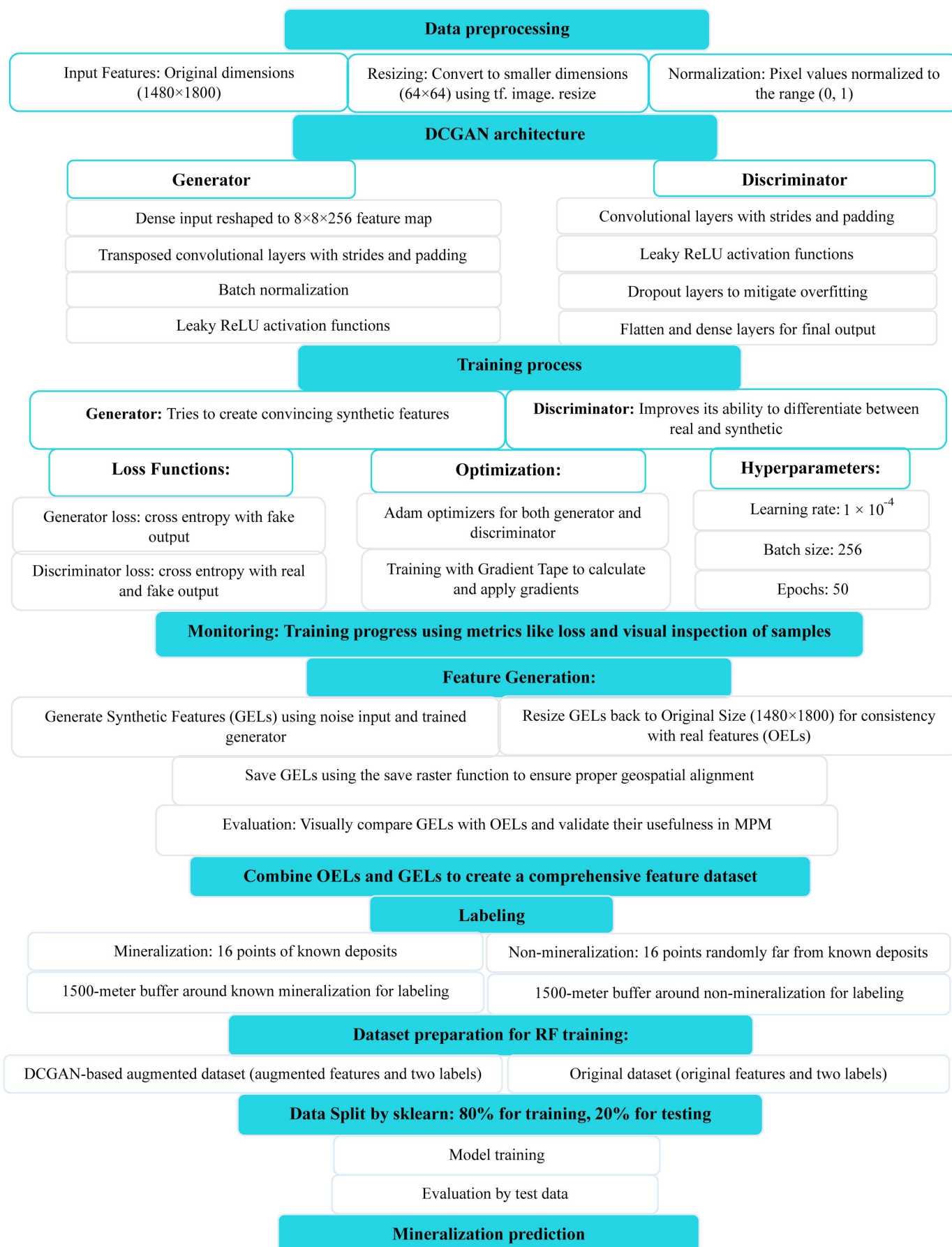**Mineralization prediction**

Figure 7. Graphical methodology of the DCGAN-based feature augmentation and RF-based mineralization prediction in this study.

In mineral exploration, the creation of predictive maps to distinguish potential areas from others requires classification to identify promising zones. There are several methods for classifying predictive maps. In this study, we used the Natural Break (NB) tool in ArcMap 10.8.1 for both prospectivity maps to determine the weighted classes, the proportion of the study area, and the proportion of known deposits in each class. Tables 2 and 3 show the distribution of probability classes and the proportion of known mineral occurrences in the prospectivity maps created with RF based on real features and DCGAN-based enhanced features.

Table 2. Distribution of probability classes and proportion of known mineral deposits through prospectivity map obtained by RF based on real features.

Classes Based on the Natural Break Tool	Number of Cells	Proportion of the Study Area (%)	Known Deposit Occupied	Proportion of Known Deposit (%)
0–0.09	52,665	58	0	0
0.09–0.30	12,387	14	0	0
0.30–0.57	5076	6	2	12.5
0.57–0.84	5124	7	5	31.25
0.84–1	8187	9	9	56.25

Table 3. Distribution of probability classes and proportion of known mineral deposits through prospectivity map obtained by RF based on DCGAN-based feature augmentation approach.

Classes Based on the Natural Break Tool	Number of Cells	Proportion of the Study Area (%)	Known Deposit Occupied	Proportion of Known Deposit (%)
0–0.05	58,509	64	0	0
0.05–0.20	15,338	17	0	0
0.20–0.50	3102	3	1	6.25
0.50–0.82	6660	7	5	31.25
0.82–1	7695	8	10	62.5

6. Discussion

Although powerful ML and DL methods are widely used in various sciences, including mineral exploration [10–14,40,86,90,91], they are still in the early stages of development. This indicates potential for growth, leading to more realistic and authentic results, especially in the forecasting literature. Many studies have successfully used DL algorithms to identify areas with high mineralization potential. However, these artificial intelligence methods can be further improved with innovative ideas.

This study focused on enhancing mineralization prediction through the introduction of a novel data augmentation method utilizing DCGAN-based feature augmentation. By generating new evidence layers as informative features aligned with underlying geological patterns, this approach significantly improved the predictive capability of the model. The augmented features are consistent with real features and provide efficient information from complex geological patterns, ultimately increasing the reliability of predictions and facilitating confident mapping of MVT Pb-Zn mineralization. Additionally, the evaluation metrics revealed that the proposed model, enhanced by DCGAN-based feature augmentation, achieved an R^2 score of 0.92 and an AUPRC of 0.99. In contrast, the model trained solely on existing features obtained an R^2 score of 0.87 and an AUPRC of 0.98. These findings underscore the robustness of the proposed model and highlight how the innovative feature augmentation method contributed to improve predictive capabilities. The RF model trained with augmented features exhibited higher accuracy in identifying mineralization areas compared to the model trained solely on real features.

The final prospectivity map generated with the proposed method demonstrated broader coverage of known MVT Pb-Zn mineralization deposits, indicating its effectiveness. Tables 2 and 3 provide a clear overview of the distribution of probability classes based on the NB classification tool, matched to the proportion of the study area and known mineral occurrences occupied by each class. These tables illustrate how the study area is divided into different probability classes and how these classes relate to the known mineral occurrences. This is crucial for understanding the spatial distribution of mineral occurrences. Indicating the proportion of the study area and the proportion of known deposits helps to illustrate the effectiveness of each probability class in identifying mineral occurrences. The breakdown into specific classes allows a detailed analysis of how different probability ranges contribute to the identification of mineral occurrences. Table 3 shows that the prediction map created using the DCGAN-based data augmentation technique covered all known deposits in only 18% of the study area, while the predictive map based on real features occupied 22% of the study area and covered all known deposits.

The findings of this study advocate for the use of innovative feature augmentation techniques, such as DCGAN-based methods, to advance the accuracy and efficiency of mineral exploration models. By successfully integrating these methodologies, we can achieve more effective identification of potential mineralization zones, paving the way for future research and exploration efforts.

7. Conclusions

This research focused on advancing the geological understanding of Mississippi Valley-type (MVT) Pb-Zn mineralization through the creation of new evidence layers as informative features. By aligning these features with actual geological data, we were able to extract valuable insights from complex geological patterns, significantly enhancing the reliability of predictions and the confidence in mapping mineralization. The results demonstrated that the mineralization prediction map generated using the proposed Deep Convolutional Generative Adversarial Network (DCGAN)-based data augmentation method covered a greater proportion of known deposits within a smaller area compared to the map based solely on real features. Specifically, the DCGAN approach achieved complete coverage of known deposits over just 18% of the study area. This detailed analysis underscores the effectiveness of the proposed method in accurately identifying regions with high mineralization potential.

In conclusion, the innovative application of data augmentation techniques in this study has proven to be a significant advancement in enhancing the accuracy and reliability of mineralization predictions. Future research should continue to explore and refine these methods, incorporating additional geoscience data to further enhance predictive capabilities in mineral exploration. By doing so, we can improve our understanding of mineralization processes and contribute to more successful exploration strategies.

Author Contributions: Conceptualization, S.Q.; Methodology, S.Q.; Software, S.Q.; Validation, S.Q., A.M., A.B.P., A.R. and M.Y.; Formal analysis, S.Q.; Investigation, S.Q.; Resources, S.Q. and A.M.; Data curation, S.Q. and A.M.; Writing—Original Draft Preparation, S.Q.; Writing—Review & Editing, S.Q., A.M. and A.B.P.; Visualization, S.Q.; Supervision, A.M.; Project administration, A.M. All authors have read and agreed to the published version of the manuscript.

Data Availability Statement: The data used in this study can be accessed upon reasonable request from the corresponding author.

References

1. Lou, Y.; Liu, Y. Mineral Prospectivity Mapping Based on a Novel Self-Ensembling Graph Convolutional Network. *Math. Geosci.* **2025**. [CrossRef]

2. Liu, Y.; Cheng, Q.; Xia, Q.; Wang, X. Mineral potential mapping for tungsten polymetallic deposits in the Nanling metallogenic belt, South China. *J. Earth Sci.* **2014**, *25*, 689–700. [CrossRef]

3. Liu, Y.; Xia, Q.; Cheng, Q. Aeromagnetic and geochemical signatures in the Chinese Western Tianshan: Implications for tectonic setting and mineral exploration. *Nat. Resour. Res.* **2021**, *30*, 3165–3195. [CrossRef]

4. Parsa, M.; Maghsoudi, A.; Yousefi, M.; Carranza, E.J. Multifractal interpolation and spectrum–area fractal modeling of stream sediment geochemical data: Implications for mapping exploration targets. *J. Afr. Earth Sci.* **2017**, *128*, 5–15. [CrossRef]

5. Ghasemzadeh, S.; Maghsoudi, A.; Yousefi, M.; Mihalasky, M.J. Information value-based geochemical anomaly modeling: A statistical index to generate enhanced geochemical signatures for mineral exploration targeting. *Appl. Geochem.* **2022**, *136*, 105177. [CrossRef]

6. Saremi, M.; Maghsoudi, A.; Ghezelbash, R.; Yousefi, M.; Hezarkhani, A. Targeting of porphyry copper mineralization using a continuous-based logistic function approach in the Varzaghan district, north of Urumieh-Dokhtar magmatic arc. *J. Min. Environ.* **2024**. [CrossRef]

7. Saremi, M.; Maghsoudi, A.; Hoseinzade, Z.; Mokhtari, A.R. Data-driven AHP: A novel method for porphyry copper prospectivity mapping in the Varzaghan District, NW Iran. *Earth Sci. Inform.* **2024**, *17*, 5063–5078. [CrossRef]

8. Zuo, R.; Xiong, Y.; Wang, Z.; Wang, J.; Kreuzer, O.P. A new generation of artificial intelligence algorithms for mineral prospectivity mapping. *Nat. Resour. Res.* **2023**, *32*, 1859–1869. [CrossRef]

9. Zuo, R.; Cheng, Q.; Xu, Y.; Yang, F.; Xiong, Y.; Wang, Z.; Kreuzer, O.P. Explainable artificial intelligence models for mineral prospectivity mapping. *Sci. China Earth Sci.* **2024**, *67*, 2864–2875. [CrossRef]

10. Shirazi, A.; Hezarkhani, A.; Shirazy, A.; Pour, A.B. Geochemical modeling of copper mineralization using geostatistical and machine learning algorithms in the Sahlabad area, Iran. *Minerals* **2023**, *13*, 1133. [CrossRef]

11. Hajihosseinlou, M.; Maghsoudi, A.; Ghezelbash, R. A novel scheme for mapping of MVT-type Pb–Zn prospectivity: LightGBM, a highly efficient gradient boosting decision tree machine learning algorithm. *Nat. Resour. Res.* **2023**, *32*, 2417–2438. [CrossRef]

12. Zuo, R.; Carranza, E.J. Machine learning-based mapping for mineral exploration. *Math. Geosci.* **2023**, *55*, 891–895. [CrossRef]

13. Mou, N.; Carranza, E.J.; Wang, G.; Sun, X. A framework for data-driven mineral prospectivity mapping with interpretable machine learning and modulated predictive modeling. *Nat. Resour. Res.* **2023**, *32*, 2439–2462. [CrossRef]

14. Xu, Y.; Zuo, R. Spatial-spectrum two-branch model based on a superpixel graph convolutional network and 1DCNN for geochemical anomaly identification. *Math. Geosci.* **2024**. [CrossRef]

15. Parsa, M.; Carranza, E.J. Modulating the impacts of stochastic uncertainties linked to deposit locations in data-driven predictive mapping of mineral prospectivity. *Nat. Resour. Res.* **2021**, *30*, 3081–3097. [CrossRef]

16. Zuo, R.; Kreuzer, O.P.; Wang, J.; Xiong, Y.; Zhang, Z.; Wang, Z. Uncertainties in GIS-based mineral prospectivity mapping: Key types, potential impacts and possible solutions. *Nat. Resour. Res.* **2021**, *30*, 3059–3079. [CrossRef]

17. Daviran, M.; Parsa, M.; Maghsoudi, A.; Ghezelbash, R. Quantifying uncertainties linked to the diversity of mathematical frameworks in knowledge-driven mineral prospectivity mapping. *Nat. Resour. Res.* **2022**, *31*, 2271–2287. [CrossRef]

18. Yang, F.; Wang, Z.; Zuo, R.; Sun, S.; Zhou, B. Quantification of uncertainty associated with evidence layers in mineral prospectivity mapping using direct sampling and convolutional neural network. *Nat. Resour. Res.* **2022**, *32*, 79–98. [CrossRef]

19. Yousefi, M.; Lindsay, M.D.; Kreuzer, O. Mitigating uncertainties in mineral exploration targeting: Majority voting and confidence index approaches in the context of an exploration information system (EIS). *Ore Geol. Rev.* **2024**, *165*, 105930. [CrossRef]

20. Lin, N.; Chen, Y.; Liu, H.; Liu, H. A comparative study of machine learning models with hyperparameter optimization algorithm for mapping mineral prospectivity. *Minerals* **2021**, *11*, 159. [CrossRef]

21. Fan, M.; Xiao, K.; Sun, L.; Zhang, S.; Xu, Y. Automated hyperparameter optimization of gradient boosting decision tree approach for gold mineral prospectivity mapping in the Xiong'ershan area. *Minerals* **2022**, *12*, 1621. [CrossRef]

22. Ghezelbash, R.; Maghsoudi, A.; Shamekhi, M.; Pradhan, B.; Daviran, M. Genetic algorithm to optimize the SVM and K-means algorithms for mapping of mineral prospectivity. *Neural Comput. Appl.* **2022**, *35*, 719–733. [CrossRef]

23. Pradhan, B.; Jena, R.; Talukdar, D.; Mohanty, M.; Sahu, B.K.; Raul, A.K.; Abdul Maulud, K. A new method to evaluate gold mineralisation-potential mapping using deep learning and an explainable artificial intelligence (XAI) model. *Remote Sens.* **2022**, *14*, 4486. [CrossRef]

24. Daviran, M.; Ghezelbash, R.; Niknezhad, M.R.; Maghsoudi, A.; Ghaeminejad, H. Hybridizing K-means clustering algorithm with harmony search and artificial bee colony optimizers for intelligence mineral prospectivity mapping. *Earth Sci. Inform.* **2023**, *16*, 2143–2165. [CrossRef]

25. Shorten, C.; Khoshgoftaar, T.M. A Survey on Image Data Augmentation for Deep Learning. *J. Big Data* **2019**, *6*, 60. [CrossRef]

26. Alzubaidi, L.; Zhang, J.; Humaidi, A.J.; Al-dujaili, A.; Duan, Y.; Al-Shamma, O.; Santamaría, J.I.; Fadhel, M.A.; Al-Amidie, M.; Farhan, L. Review of Deep Learning: Concepts, CNN Architectures, Challenges, Applications, Future Directions. *J. Big Data* **2021**, *8*, 53. [CrossRef]

27. Talaei Khoei, T.; Ould Slimane, H.; Kaabouch, N. Deep Learning: Systematic Review, Models, Challenges, and Research Directions. *Neural Comput. Appl.* **2023**, *35*, 23103–23124. [CrossRef]

28. Goodfellow, I.; Pouget-Abadie, J.; Mirza, M.; Xu, B.; Warde-Farley, D.; Courville, A.; Ozair, S.; Bengio, Y. Generative adversarial nets. *Adv. Neural Inf. Process. Syst.* **2014**, *27*, 2672–2680. [CrossRef]

29. Wu, E.; Wu, K.; Cox, D.; Lotter, W. Conditional infilling GANs for data augmentation in mammogram classification. In *Image Analysis for Moving Organ, Breast, and Thoracic Images*; Springer: Cham, Switzerland, 2018; pp. 98–106.

30. Frid-Adar, M.; Diamant, I.; Klang, E.; Amitai, M.; Goldberger, J.; Greenspan, H. GAN-based synthetic medical image augmentation for increased CNN performance in liver lesion classification. *Neurocomputing* **2018**, *321*, 321–331. [CrossRef]

31. Huang, H.; Yu, P.; Wang, C. An introduction to image synthesis with generative adversarial nets. *arXiv* **2018**, arXiv:1803.04469. [CrossRef]

32. Li, T.; Zuo, R.; Zhao, X.; Zhao, K. Mapping prospectivity for regolith-hosted REE deposits via convolutional neural network with generative adversarial network augmented data. *Ore Geol. Rev.* **2022**, *142*, 104693. [CrossRef]

33. Puzyrev, V.; Salles, T.; Surma, G.; Elders, C. Geophysical model generation with generative adversarial networks. *Geosci. Lett.* **2022**, *9*, 1–9. [CrossRef]

34. Stocklin, J.; Ruttner, A.; Nabavi, M. *New Data on the Lower Paleozoic and Pre-Cambrian of North Iran*; Geological Survey of Iran: Tehran, Iran, 1964; p. 1.

35. Geyer, G.; Bayet-Goll, A.; Wilmsen, M.; Mahboubi, A.; Moussavi-Harami, R. Lithostratigraphic revision of the middle Cambrian (Series 3) and upper Cambrian (Furongian) in northern and central Iran. *Newslett. Stratigr.* **2014**, *47*, 21–59. [CrossRef]

36. Khodami, M.; Shabanian, N.; Nouri Sandiani, F.; Asahara, Y.; Davoudian, A.R. A record of Late Cambrian–Early Ordovician arc magmatism in Yazd block, Central Iran. *Arab. J. Geosci.* **2022**, *15*, 876. [CrossRef]

37. Rajabi, A. *Metallogeny and Geology of Zinc-Lead Deposits with Sedimentary Host Rocks in Iran*; Univ. Tehran: Tehran, Iran, 2021.

38. Leach, D.L.; Sangster, D. Mississippi Valley-Type Lead-Zinc Deposits. In *Mineral Deposit Modeling*; Kirkham, R.V., Sinclair, W.D., Thorpe, R.I., Duke, J.M., Eds.; Geological Association of Canada Special Paper 40; Geological Association of Canada: St. John's, NL, Canada, 1993; pp. 289–314.

39. Bradley, D.; Leach, D. Tectonic controls of Mississippi Valley-type lead–zinc mineralization in orogenic forelands. *Miner. Depos.* **2003**, *38*, 652–667. [CrossRef]

40. Qaderi, S.; Maghsoudi, A.; Pour, A.B.; Yousefi, M. Geological Controlling Factors on Mississippi Valley-Type Pb-Zn Mineralization in Western Semnan, Iran. *Minerals* **2024**, *14*, 957. [CrossRef]

41. Bazargani-Guilani, K.; Faramarzi, M.; Tak, M.A. Multistage dolomitization in the Cretaceous carbonates of the east Shahmirzad area, north Semnan, central Alborz, Iran. *Carbonates Evaporites* **2010**, *25*, 177–191. [CrossRef]

42. Bazargani-Guilani, K.; Nekouvaght Tak, M.A.; Faramarzi, M. Pb–Zn deposits in Cretaceous carbonate host rocks, northeast Shahmirzad, central Alborz, Iran. *Aust. J. Earth Sci.* **2011**, *58*, 297–307. [CrossRef]

43. Bazargani-Guilani, K.; Rabiei, M.; Mehrabi, B. Effects of host rock mineralogical composition and sedimentary facies on development of geochemical halos in Shahmirzad Pb-Zn deposits, central Alborz, Iran. *J. Geochem. Explor.* **2013**, *124*, 155–165. [CrossRef]

44. Rajabi, A.; Rastad, E.; Canet, C. Metallogeny of Cretaceous carbonate-hosted Zn–Pb deposits of Iran: Geotectonic setting and data integration for future mineral exploration. *Int. Geol. Rev.* **2012**, *54*, 1649–1672. [CrossRef]

45. Rajabi, A.; Rastad, E.; Canet, C. Metallogeny of Permian–Triassic carbonate-hosted Zn–Pb and F deposits of Iran: A review for future mineral exploration. *Aust. J. Earth Sci.* **2013**, *60*, 197–216. [CrossRef]

46. Chen, Y.; Wu, W. Application of one-class support vector machine to quickly identify multivariate anomalies from geochemical exploration data. *Geochem. Explor. Environ. Anal.* **2017**, *17*, 231–238. [CrossRef]

47. Grunsky, E.; Caritat, P.D. State-of-the-Art Analysis of Geochemical Data for Mineral Exploration. *Geochem. Explor. Environ. Anal.* **2019**, *20*, geochem2019-031. [CrossRef]

48. Li, H.; Li, X.; Yuan, F.; Jowitt, S.; Zhang, M.; Zhou, J.; Zhou, T.; Li, X.; Ge, C.; Wu, B. Convolutional neural network and transfer learning based mineral prospectivity modeling for geochemical exploration of Au mineralization within the Guandian–Zhangbaling area, Anhui Province, China. *Appl. Geochem.* **2020**, *122*, 104747. [CrossRef]

49. Parsa, M.; Maghsoudi, A. Controls on Mississippi Valley-Type Zn-Pb mineralization in Behabad district, Central Iran: Constraints from spatial and numerical analyses. *J. Afr. Earth Sci.* **2018**, *140*, 189–198. [CrossRef]

50. Gibson, G.M.; Edwards, S. Basin inversion and structural architecture as constraints on fluid flow and Pb–Zn mineralization in the Paleo–Mesoproterozoic sedimentary sequences of northern Australia. *Solid Earth* **2020**, *11*, 1205–1226. [CrossRef]

51. Ferrill, D.A.; Smart, K.J.; Morris, A.P. Resolved stress analysis, failure mode, and fault-controlled fluid conduits. *Solid Earth* **2020**, *11*, 899–908. [CrossRef]

52. Bowness, N.P.; Cawood, A.J.; Ferrill, D.A.; Smart, K.J.; Bellow, H.B. Mineralogy controls fracture containment in mechanically layered carbonates. *Geol. Mag.* **2023**, *159*, 1855–1873. [CrossRef]

53. Berman, M. Distance distributions associated with poisson processes of geometric figures. *J. Appl. Probab.* **1977**, *14*, 195–199. [CrossRef]

54.   Gorum, T.; Carranza, E.J.M. Control of style-of-faulting on spatial pattern of earthquake-triggered landslides. *Int. J. Environ. Sci. Technol.* **2015**, *12*, 3189–3212. [CrossRef]

55.   Nguemhe Fils, S.C.; Mimba, M.; Nyeck, B.; Nforba, M.; Boniface, K.; Nouck, P.; Hell, J. GIS-Based Spatial Analysis of Regional-Scale Structural Controls on Gold Mineralization Along the Bétaré-Oya Shear Zone, Eastern Cameroon. *Nat. Resour. Res.* **2020**, *29*, 3457–3477. [CrossRef]

56.   Zeeh, S.; Bechstädt, T. Carbonate-Hosted Pb-Zn Mineralization at Bleiberg-Kreuth (Austria): Compilation of Data and New Aspects. In *Sediment-Hosted Zn-Pb Ores*; Fontboté, L., Boni, M., Eds.; Special Publication of the Society for Geology Applied to Mineral Deposits; Springer: Berlin/Heidelberg, Germany, 1994; Volume 10, pp. 165–184. [CrossRef]

57.   Hosseini-Dinani, H.; Yazdi, M. Multi-dataset analysis to assess mineral potential of MVT-type zinc-lead deposits in Malayer-Isfahan metallogenic belt, Iran. *Arab. J. Geosci.* **2021**, *14*, 673. [CrossRef]

58.   He, Z.; Gao, J.; Li, S.; He, S. Mineralization of MVT Pb-Zn Deposits in the Process of Hydrocarbon Accumulation and Destruction in the Strong Structural Deformation Area of Eastern Sichuan, South China. *Minerals* **2022**, *12*, 1281. [CrossRef]

59.   Guan, G.; Li, S.; Li, R. Mineralization Process of MVT Zn-Pb Deposit Promoted by the Adsorbed Hydrocarbon: A Case Study from Mayuan Deposit on the North Margin of Sichuan Basin. *Minerals* **2023**, *13*, 72. [CrossRef]

60.   Navarro-Ciurana, D.; Corral, I.; Corbella, M. A tool for Zn-Pb MVT exploration by combining C and O isotopes and REE geochemistry of dolomite. *Ore Geol. Rev.* **2023**, *156*, 105405. [CrossRef]

61.   Pour, A.B.; Hashim, M.; Genderen, J.L. Detection of hydrothermal alteration zones in a tropical region using satellite remote sensing data: Bau Goldfield, Sarawak, Malaysia. *Ore Geol. Rev.* **2013**, *54*, 181–196. [CrossRef]

62.   Pour, A.B.; Park, Y.; Crispini, L.; Läufer, A.; Hong, J.K.; Park, T.S.; Zoheir, B.; Pradhan, B.; Muslim, A.M.; Hossain, M.S.; et al. Mapping Listvenite Occurrences in the Damage Zones of Northern Victoria Land, Antarctica Using ASTER Satellite Remote Sensing Data. *Remote Sens.* **2019**, *11*, 1408. [CrossRef]

63.   Crósta, A.P.; de Souza Filho, C.R.; Azevedo, F.; Brodie, C. Targeting key alteration minerals in epithermal deposits in Patagonia, Argentina, using ASTER imagery and principal component analysis. *Int. J. Remote Sens.* **2003**, *24*, 4233–4240. [CrossRef]

64.   Gabr, S.S.; Ghulam, A.; Kusky, T.M. Detecting areas of high-potential gold mineralization using ASTER data. *Ore Geol. Rev.* **2010**, *38*, 59–69. [CrossRef]

65.   Pour, A.B.; Park, T.S.; Park, Y.; Hong, J.K.; Zoheir, B.; Pradhan, B.; Ayoobi, I.; Hashim, M. Application of Multi-Sensor Satellite Data for Exploration of Zn-Pb Sulfide Mineralization in the Franklinian Basin, North Greenland. *Remote Sens.* **2018**, *10*, 1186. [CrossRef]

66.   Abubakar, A.J.; Hashim, M.; Pour, A.B. Identification of hydrothermal alteration minerals associated with geothermal system using ASTER and Hyperion satellite data: A case study from Yankari Park, NE Nigeria. *Geocarto Int.* **2019**, *34*, 597–625. [CrossRef]

67.   Sekandari, M.; Masoumi, I.; Pour, A.B.; Muslim, A.M.; Hossain, M.S.; Misra, A. ASTER and WorldView-3 satellite data for mapping lithology and alteration minerals associated with Pb-Zn mineralization. *Geocarto Int.* **2020**, *37*, 1782–1812. [CrossRef]

68.   Aali, A.A.; Shirazy, A.; Shirazi, A.; Pour, A.B.; Hezarkhani, A.; Maghsoudi, A.; Hashim, M.; Khakmardan, S. Fusion of Remote Sensing, Magnetometric, and Geological Data to Identify Polymetallic Mineral Potential Zones in Chakchak Region, Yazd, Iran. *Remote Sens.* **2022**, *14*, 6018. [CrossRef]

69.   Hajaj, S.; El Harti, A.; Jellouli, A.; Pour, A.B.; Himyari, S.M.; Hamzaoui, A.; Bensalah, M.K.; Benaouiss, N.; Hashim, M. HyMap imagery for copper and manganese prospecting in the east of Ameln valley shear zone (Kerdous inlier, western Anti-Atlas, Morocco). *J. Spat. Sci.* **2023**, *69*, 81–102. [CrossRef]

70.   Pour, B.A.; Hashim, M. The application of ASTER remote sensing data to porphyry copper and epithermal gold deposits. *Ore Geol. Rev.* **2012**, *44*, 1–9. [CrossRef]

71.   Carranza, E.J.M.; Hale, M. Where are porphyry copper deposits spatially localized? A case study in Benguet province, Philippines. *Nat. Resour. Res.* **2002**, *11*, 45–59. [CrossRef]

72.   Bishop, C.M. *Pattern Recognition and Machine Learning*; Springer Science Business Media: New York, NY, USA, 2006.

73.   Carranza, E.J.M. Geochemical Anomaly and Mineral Prospectivity Mapping in GIS. In *Handbook of Exploration and Environmental Geochemistry*; Elsevier: Amsterdam, The Netherlands, 2008; Volume 11.

74.   Theodoridis, S.; Koutroumbas, K. Clustering: Basic concepts. *Pattern Recogn.* **2009**, 595–625. [CrossRef]

75.   Yousefi, M.; Kamkar-Rouhani, A.; Carranza, E.J.M. Geochemical mineralization probability index (GMPI): A new approach to generate enhanced stream sediment geochemical evidential map for increasing probability of success in mineral potential mapping. *J. Geochem. Explor.* **2012**, *115*, 24–35. [CrossRef]

76.   Yousefi, M.; Kamkar-Rouhani, A.; Carranza, E.J.M. Application of staged factor analysis and logistic function to create a fuzzy stream sediment geochemical evidence layer for mineral prospectivity mapping. *Geochem. Explor. Environ. Anal.* **2013**, *14*, 45–58. [CrossRef]

77.   Mutele, L.; Billay, A.; Hunt, J.P. Knowledge-Driven Prospectivity Mapping for Granite-Related Polymetallic Sn–F–(REE) mineralization, Bushveld Igneous Complex, South Africa. *Nat. Resour. Res.* **2017**, *26*, 535–552. [CrossRef]

78.   Nykänen, V.; Törmänen, T.; Niiranen, T. Cobalt Prospectivity Using a Conceptual Fuzzy Logic Overlay Method Enhanced with the Mineral Systems Approach. *Nat. Resour. Res.* **2023**, *32*, 2387–2416. [CrossRef]

79. Brownlee, J. A Tour of Generative Adversarial Network Models. *Machine Learning Mastery*. 2019. Available online: https://machinelearningmastery.com/tour-of-generative-adversarial-network-models/ (accessed on 12 July 2019).

80. Zhao, G.; Cai, Z.; Wang, X.; Dang, X. GAN Data Augmentation Methods in Rock Classification. *Appl. Sci.* **2023**, *13*, 5316. [CrossRef]

81. Ahmad, Z.; Jaffri, Z.U.; Chen, M.; Bao, S. Understanding GANs: Fundamentals, variants, training challenges, applications, and open problems. *Multimed. Tools Appl.* **2024**. [CrossRef]

82. Breiman, L.; Friedman, J.H.; Olshen, R.A.; Stone, C.J. Classification and Regression Trees. *Biometrics* **1984**, *40*, 874.

83. Breiman, L. Random Forests. *Mach. Learn.* **2001**, *45*, 5–32. [CrossRef]

84. Carranza, E.J.; Laborte, A.G. Data-driven predictive mapping of gold prospectivity, Baguio district, Philippines: Application of Random Forests algorithm. *Ore Geol. Rev.* **2015**, *71*, 777–787. [CrossRef]

85. Xiang, J.; Xiao, K.; Carranza, E.J.; Chen, J.; Li, S. 3D Mineral Prospectivity Mapping with Random Forests: A Case Study of Tongling, Anhui, China. *Nat. Resour. Res.* **2019**, *29*, 395–414. [CrossRef]

86. Bigdeli, A.; Maghsoudi, A.; Ghezelbash, R. Recognizing Geochemical Anomalies Associated with Mineral Resources Using Singularity Analysis and Random Forest Models in the Torud-Chahshirin Belt, Northeast Iran. *Minerals* **2023**, *13*, 1399. [CrossRef]

87. CERN. "Probability Density Functions (PDF)." ROOT, CERN. Available online: https://root.cern.ch/doc/v608/group__PdfFunc.html (accessed on 25 December 2024).

88. Cohen, J. Statistical Power Analysis for the Behavioral Sciences. In *The SAGE Encyclopedia of Research Design*; SAGE Publications: Thousand Oaks, CA, USA, 1969.

89. Wen, P.; Xu, Q.; Yang, Z.; He, Y.; Huang, Q. Exploring the Algorithm-Dependent Generalization of AUPRC Optimization with List Stability. *arXiv* **2022**, arXiv:abs/2209.13262.

90. Adler, A.; Araya-Polo, M.; Poggio, T.A. Deep Learning for Seismic Inverse Problems: Toward the Acceleration of Geophysical Analysis Workflows. *IEEE Signal Process. Mag.* **2021**, *38*, 89–119. [CrossRef]

91. Sun, Y.; Araya-Polo, M.; Williamson, P. Data characterization and transfer learning for DL-driven velocity model building. In *First International Meeting for Applied Geoscience & Energy Expanded Abstracts*; Society of Petroleum Engineers: Richardson, TX, USA, 2021.